

# Segment aberration effects on contrast

Ian J. Crossfield and Mitchell Troy

*Jet Propulsion Laboratory, California Institute of Technology*

*4800 Oak Grove Dr., Pasadena, CA 91109*

*Ian.J.Crossfield@jpl.nasa.gov*

High-contrast imaging, particularly direct detection of extrasolar planets, is a major science driver for the next generation of telescopes. This science requires the suppression of scattered starlight at extremely high levels, and telescopes must be correctly designed today to meet these stringent requirements in the future. The challenge increases in systems with complicated aperture geometries such as obscured, segmented telescopes. Such systems can also require intensive modelling and simulation efforts in order to understand the tradeoffs between different optical parameters. In this paper we describe the feasibility and development of a contrast prediction tool for use in the design and systems engineering of these telescopes. We describe analytically the performance of a particular starlight suppression system on a large segmented telescope. These analytical results and the results of our contrast predictor are then compared to the results of a full wave-optics simulation. © 2007 Optical Society of America

## 1. INTRODUCTION

In the last fifteen years there has been an eruption of interest in the field of extrasolar planetary astronomy. Since the discovery of the first extrasolar planet around a sunlike star by Mayor & Queloz,<sup>1</sup> nearly two hundred extrasolar planets (also called exoplanets) have been found. These exoplanets have been found with several different search methods, including radial velocity, transit, and gravitational microlensing.

Excitingly, the last few years may have seen the first tantalizing glimpses of directly-imaged exoplanets.<sup>2</sup> Despite these tantalizing discoveries, the vast majority of known exoplanets have been detected only indirectly; that is, their presence has been inferred but exoplanetary photons have not been measured. Thus indirect detection precludes most characterization, limiting what we can indirectly learn about an exoplanet. In addition, these few imaged candidates all orbit cool (K or M) stars and are all widely separated on the sky from their parent stars. Thus the goal of imaging solar system analogues remains unattained.

For this reason there are a number of efforts underway to image planets from both ground and space observatories. In all efforts the ultimate goal can only be achieved by sufficiently suppressing the light from the parent star so that any companion exoplanets can be detected. While young “hot Jupiters”<sup>3</sup> are visible at a contrast of  $10^{-6}$ , reflected-light Jovians<sup>4</sup> require contrasts of  $10^{-8}$  and terrestrial planets<sup>5</sup> a

demanding  $10^{-10}$ .

A variety of suppression methods have been proposed to successfully perform this imaging. A distinguishing feature of the current astronomical efforts is that they all utilize monolithic telescopes. In general, the starlight suppression systems proposed all tend to perform best in the absence of entry pupil amplitude variations such as segment gaps. The most ambitious such project, the Terrestrial Planet Finder Coronagraph, uses an unobscured off-axis design to achieve maximum performance.

However, the next generation of observatories – the James Webb Space Telescope, the Thirty Meter Telescope, the European Extremely Large Telescope, and others – will follow in the footsteps of the Keck Observatory by using segmented mirror designs with substantial obscurations. The quality of segmented optics adds an additional layer of complexity to an optical prescription. While it is often convenient to describe the optical properties of a monolithic optic in terms of global aberration modes, in a segmented telescope aberrations defined on the segments also become important. The optical quality of the segments can strongly influence the final telescope performance in a way not easily described with standard global aberrations.

In Section 2 we describe the use of a nulling interferometer to suppress the starlight and develop the necessary nomenclature. We also discuss the linearity of such a system and how this feature can make useful predictions. Section 3 describes a wave-optics simulation with the goal of quickly predicting achieved contrast. Finally, in Section 4 we predict the contrast for several cases of complicated segment aberrations and

compare these predictions to the contrast measured in a full simulation.

## 2. ANALYTICAL ANALYSIS OF SEGMENT ERRORS

We begin by describing the wavefront from an aberrated segmented system, and then discuss how this system behaves when used with a visible shearing nuller.<sup>6</sup> One advantage a nuller has over many other proposed suppression systems is that with proper design it can obviate any performance degradation from pupil obscurations, including segment gaps.

### 2.A. Segmented Apertures

Let a plane wave of unit amplitude be incident on a segmented aperture. After reflection the electric field may be defined by the sum of the electric fields over all  $N$  segments in the aperture

$$E(x, y) = \sum_{n=1}^N E_n(\vec{x} - \vec{r}_n) \quad (1)$$

$E_n$  is the complex field resulting from the segment centered at  $\vec{r}_n$ , the  $n^{\text{th}}$  position.

We define a segment's shape function as  $\theta(x, y)$  – which equals unity inside the segment and zero outside – and ignore amplitude errors such as mirror reflectivity variations. Since in the absence of global aberrations each segment's phase errors are independent, we write the field resulting from the  $n^{\text{th}}$  segment as

$$E_n(\vec{x} - \vec{r}_n) = \theta(\vec{x} - \vec{r}_n) \exp [j\phi_n(\vec{x} - \vec{r}_n)] \quad (2)$$

We can decompose the segment phase aberrations using a set of basis functions defined on the segment. This means that we can write the aberrations of a single segment as

$$\phi_n(\vec{x} - \vec{r}_n) = \sum_{k=1} c_{nk} Z_k(\vec{x} - \vec{r}_n) \quad (3)$$

where  $c_{nk}$  is the coefficient of the  $k^{\text{th}}$  basis function on the  $n^{\text{th}}$  segment, and  $Z_k$  is the functional representation of that mode.

### *2.B. Segmented Nulling*

A nulling interferometer an input pupil into two beams and adds a  $\pi$  phase shift to one beam. One beam is then sheared a distance  $s$  and the beams are recombined to destructively interfere the central, overlapping region, as shown in Figure 1 (a). The bright outer portion of the recombined field is then masked out with a Lyot stop. The nulled central portion of the field passes through the Lyot stop and is brought to focus on a detector.

At the cost of throughput in the Lyot stop, one can improve the contrast sensitivity by splitting and re-interfering the nulled pupil with itself a second time. As originally conceived, the two shears are perpendicular to each other as shown in Figure 1 (b).<sup>6</sup> However, in general the second shear can be in any direction. We consider below a second type of nuller in which both shears are parallel; we call this a parallel dual-shear nuller. This last variation is shown in Figure 1 (c).

If not properly corrected, the optical gaps of a segmented aperture will significantly

degrade a nuller's performance by allowing light to leak through. This leakage can be ameliorated by either blocking the gap locations with a reticulated stop, or by setting the shear distance  $s$  to be an integral number of segment widths. When this condition is satisfied the segments and their associated gaps precisely overlap in the overlaid pupils and the gap leakage is eliminated. The complex field at each segment position is then the result of the interferometric nulling of several segments' fields. The nulled field at the position  $r_m^{\vec{}}$  (where the set of  $m$  consists only of those  $M$  segment positions at which full nulling occurs) can therefore be written to first order as

$$E_m^{\text{null}} = j\theta_m (\vec{x} - r_m^{\vec{}}) \sum_{k=1} \chi_{mk} Z_k (\vec{x} - r_m^{\vec{}}) \quad (4)$$

where  $\chi_{mk}$  represents the nulled coefficient of the  $k^{\text{th}}$  mode at the  $m^{\text{th}}$  segment position. If the distribution of the aberration mode coefficients are known, then the expected distribution of the  $\chi_{mk}$  can also be derived; its form depends on the geometry of the nuller used. In the canonical perpendicular-shear nuller four separate segment fields are combined, and we have (to first order)

$$\chi_{mk}^{\text{perp}} = \frac{1}{4} (c_{m_1k} - c_{m_2k} + c_{m_3k} - c_{m_4k}) \quad (5)$$

In the parallel dual-shear nuller where both shears are the same magnitude and direction, one segment is combined twice with two others and we have instead

$$\chi_{mk}^{\text{lin}} = \frac{1}{2} \left[ c_{m_1k} - \frac{1}{2} (c_{m_2k} + c_{m_3k}) \right] \quad (6)$$

We can then rewrite the nulled exit pupil field as a sum of the terms of Eq. (4)

$$E_{\text{null}} = j \sum_{m=1}^M \theta_m \sum_k \chi_{mk} Z_k \quad (7)$$

And the intensity at the nulled plane is therefore given by

$$I_{\text{null}} = \sum_{m=1}^M \theta_m \left( \sum_k Z_k \chi_{mk} \right) \left( \sum_l Z_l \chi_{ml} \right) \quad (8)$$

With a sufficiently large number of segments, this final intensity can be estimated using an ensemble average. If we use an orthogonal set of aberration functions on the segments, then by orthogonality the average of the cross-terms of Eq. (8) is zero. The intensity in the final nulled exit pupil is then

$$I_{\text{null}} = \sum_{m=1}^M \theta_m \sum_k \chi_{mk}^2 Z_k^2 \quad (9)$$

If the coefficients of the  $k^{\text{th}}$  aberration mode are normally distributed with zero mean and variance  $\sigma_k^2$ , then  $\chi_{mk}$  will also be normally distributed, zero-mean, and have variance  $\sigma_\chi^2 = G\sigma_k^2$ . In this case  $G$  is a constant determined by the geometry of the nuller –  $G$  takes the value 0.25 for the traditional perpendicular dual-shear nuller and 0.375 for the parallel dual-shear nuller. The former’s lower sensitivity to segment aberrations results from its interference of the fields from four segments rather than three segments (as in the case of the parallel dual-shear nuller) and the aberrations are thus averaged down somewhat more. The mean intensity of light which leaks through into the nulled pupil plane is just

$$\langle I_{\text{null}} \rangle = \sum_k \sigma_{\chi_{mk}}^2 = G \sum_k \sigma_k^2 \quad (10)$$

It follows from this that in the presence of a single segment aberration, the intensity of leaked light in the nulled pupil plane is dependent only on the aberration level and not on the particular aberration term. Furthermore, this demonstrates that the final intensity in the nulled plane of a segmented system is directly proportional to the sum of the segment aberration variances. This is a useful quantity to know *a priori* for, e.g., the design of post-coronagraphic pupil-plane wavefront sensors. In addition, we expect the contrast achieved in an uncorrected image to be directly proportional to the intensity in the pupil plane. A consequence of this correlation is that there exists a dependence of contrast on wavefront error which corresponds to that described for pupil intensity in Eq. (10).

### *2.C. Corrected systems*

Any ground-based telescope used for direct exoplanet detection must work behind an adaptive optics system which partially corrects both static and dynamic wavefront errors. We therefore investigate whether a relation similar to Eq. (10) exists for an AO-corrected system.

An analytic examination of AO correction of segment piston errors by Yaitskova & Verinaud<sup>7</sup> defined the quantity  $\gamma_k$ , the amount of wavefront correction achieved by an AO system on a particular segment aberration. This correction factor is defined by the ratio of the corrected RMS wavefront error to the initial, uncorrected RMS

wavefront error:

$$\gamma_k = \frac{\sigma_{\text{corr}}}{\sigma_{\text{init}}} \quad (11)$$

In the absence of measurement or correction errors  $\gamma_k$  is independent of the initial level of wavefront error. It is, however, dependent on both the density and geometry of the deformable mirror actuators.

Assuming that there exists a set of correction factors  $\gamma_k$  for each segment aberration, we can now predict the average intensity in the AO-corrected, nulled pupil. We rewrite Eq. (10) for AO-corrected wavefronts as

$$\langle I_{\text{null}} \rangle = G \sum_k \gamma_k^2 \sigma_k^2 \quad (12)$$

Contrast estimation in a corrected system is more complicated. The typical use of wavefront correction in a high-contrast imaging system is to carve out a “dark hole” in the image plane: it is this hole which is the primary region of interest. The contrast in this region may improve by many orders of magnitude, and its improvement is not quantified by the same set of wavefront correction factors. However, if the wavefront correction is a linear process we will still be able to write the contrast as a linear system. The amount of contrast improvement for each segment aberration will decrease with increasing aberration order since, in general, aberrations with higher spatial frequency components are less correctable.

### 3. WAVE OPTICS SIMULATIONS

We conducted a number of numerical simulations to test the above derivations. We modeled a proposed high-contrast instrument on the Thirty Meter Telescope, described in Section 3.A below. We first calculate the wavefront correction factors in Section 3.C. We then compare in Section 3.D the measured light leakage to the theoretical relation in Eqs. (10) and (12), and examine the dependence of the achieved contrast to both uncorrected and corrected segment aberrations.

#### 3.A. Optical System

The TMT primary mirror is an  $f/1$  circularized array of hexagonal segments approximately 30 m in diameter. The 738 segments are 1.2 m corner to corner and have 4 mm optical gaps between them. In addition to these gaps, the TMT has a complicated obscuration geometry: the secondary mirror platform creates a 3.65 m diameter central obscuration, which is supported by three 0.5 m support struts and six 1 cm cables. The fully obscured TMT aperture can be seen in Figure 2.

The Planet Formation Instrument (PFI) is the high-contrast instrument proposed for the TMT, designed primarily for detection and characterization of extrasolar planets.<sup>4</sup> It consists of a fast, high-order frontend AO system, a shearing nuller with an additional integrated deformable mirror and backend wavefront sensor, and an Integral Field Spectrograph as the primary science instrument. The nuller is of the parallel dual-shear variety: both shears are along the same axis, of the same magnitude, and

an integral number of segment widths (3 segments, or about 3.1 m).

We simulate the telescope system using the Gray Pixel Approximation to generate grayscale apertures.<sup>8</sup> This method allows us to accurately represent the small gaps using approximately 3 cm/pixel resolution. Phase errors are applied to the segments in the form of Zernike aberrations<sup>9</sup> with normally-distributed coefficients. The resulting complex pupils are then run through an adaptive optics simulation using the Arroyo library.<sup>10</sup> The adaptive optics system is modeled as a 127x127 deformable mirror and a spatially filtered Shack-Hartmann wavefront sensor. The simulation corrects each case in a closed loop until the wavefront error has been minimized. The corrected pupil is then sent through a model of the PFI nuller described above, and the nulled pupil is subsequently imaged and the achieved contrast computed. All our simulations were monochromatic and in H band ( $1.65 \mu\text{m}$ ), the PFI's nominal operating wavelength.

### *3.B. Method Used*

In the simulation we apply one Zernike aberration at a time to the TMT segments, with the aberration coefficients drawn from a normal distribution. Several pupils are generated for each aberration term, each using different levels of wavefront error. Several realizations of each of these cases are simulated and the contrast results averaged. In all cases we report the contrast value averaged from 3-10  $\lambda/D$ , the innermost portion of PFI's working region. This analysis was performed for sets of pupils both with and without AO correction.

For each segment aberration we compute the AO correction factor using the variances of the corrected and uncorrected wavefronts. We then examine the relationships between the uncorrected RMS wavefront error and (1) the nulled pupil-plane intensity and (2) the final achieved contrast. Both the null intensity and the contrast should be proportional to the wavefront variance. We expect from Eq. (10) to see the same level of light leakage for a particular distribution of any single uncorrected segment aberration. However, we do not in general expect the contrast to be the same for different aberrations.

### *3.C. AO Correction Factors*

The correction factors  $\gamma_k$  were computed for all segment aberrations through fourth order and are plotted in Figure 3. For the AO system used the  $\gamma_k$  are independent of the initial level of wavefront error and are quite stable from one particular wavefront realization to the next. For a given radial order of segment aberration mode, the modes with lower azimuthal order are better-corrected by the adaptive optics system. The correction factor for segment piston errors, 0.40, agrees quite well with the value of 0.36 predicted analytically by Yaitskova & Verinaud for an AO system of similar order.

The fact that matching aberration modes such as the two astigmatisms (modes 5 and 6) are corrected at different levels is due to the particular geometry of the wavefront corrector used. We discuss this effect in more detail in Appendix 5. For the

reasons described in the Appendix, we hereafter combine the results of similar modes such as tip/tilt and the two astigmatisms in our plots.

### *3.D. No AO Correction*

Figure 4 shows that the theoretical intensity curve matches the measured data, and both intensity and contrast exhibit the expected  $\sigma^2$  dependences. Only the segment piston curve is shown on the intensity leakage plot because, as expected, the curve is essentially identical for all segment aberrations.

The contrast for the uncorrected case is directly proportional to the wavefront variance for all low-order segment aberrations. We note that the lower-order segment aberrations have the highest contrast sensitivity. Because low-order modes typically have the greatest magnitude,<sup>11</sup> effects such as segment misphasing and misalignment are thus likely to give the largest contributions to contrast.

As an example, the segments of the Keck telescopes are routinely phased so that the RMS segment piston is less than 12 nm wavefront.<sup>12</sup> At the TMT a similar level of phasing error in H band (1.65  $\mu\text{m}$ ) would result in a final contrast of about  $10^{-5}$ . This level of performance is wholly inadequate for the task of imaging (much less characterizing) exoplanets. This underscores the necessary role of significant further wavefront correction systems in achieving high contrast ratios.

### *3.E. With AO Correction*

We now examine the utility of the high-order adaptive optics system described in Section 3.A in improving the contrast achieved with segment aberrations. Figure 5 shows the intensity leakage and average contrast achieved for the first several low-order segment aberrations. The figure also compares the measured intensity leakage to the theoretical predictions from Eq. (12) (using the AO correction factors).

The figure shows that Eq. (12) is a reasonably good estimate of the actual intensity. As expected, the contrast improves most for lower-order segment aberrations. For example, while the contrast resulting from segment piston errors improves by roughly a factor of one thousand for a given level of wavefront error, the contribution of segment astigmatism is reduced by only roughly a factor of one hundred. Thus the relative contrast sensitivities of the segment aberrations is reversed after wavefront correction: before correction lower-order modes degrade contrast more, but because those same modes are better-corrected they hurt contrast less after correction. Note that with larger initial wavefront errors the effect is no longer linear; this is expected and due to the increasing impact of higher-order effects within the dark hole.<sup>13</sup>

Also, contrast no longer appears to be dependent on the pre-correction wavefront variance, but rather demonstrates a dependence on wavefront error that slowly increases with the amount of wavefront error. We propose that this is due to the increasing effect of higher-order terms within the dark hole.

## 4. COMPARISON OF RESULTS

In this section we discuss the results of the simulations of the systems described in Section 3. We use these results in Section 4.A to predict the resultant contrast from more complicated cases of segment aberrations and compare them against simulation results.

### 4.A. Contrast Prediction

In a previous work we described the results of a study of the effects of segment errors aberrations on contrast with the TMT PFI.<sup>11</sup> The study, though useful in designing the TMT segments to permit future high-contrast imaging, was also a time-intensive endeavor that cannot be quickly repeated each time the telescope design evolves. We therefore introduce a parameterized contrast estimator based on the observed correlation between wavefront error and contrast. This estimator takes the form

$$C = \sum_{k=1}^K \alpha_k \sigma_k^2 \quad (13)$$

By computing a fit to the curve of each segment aberration, this relation can then be used to predict the contrast from any combination of segment aberrations.

We computed the  $\alpha_k$  coefficients by fitting to the linear portion of the contrast curves in Figure 5; these coefficients are plotted in Table 1 for the all Zernike modes through fourth order. In conjunction with Eq. (13), these coefficients are all that are necessary to predict the effect of segment errors on the TMT's contrast performance.

We use this method to predict contrast and compare the prediction in Table 2 to the values for the three cases previously examined. These are the cases of (1) segment misphasing and misalignments, (2) “unwarped” segment surfaces, and (3) “warped” segments. The segment misalignment errors consist of segment piston errors of 12 nm RMS and segment tip/tilts of 6 nm RMS each. The “unwarped” case represents segments whose optical quality meets the desired surface specifications, but which have had no other correction. The “warped” segments have been statically corrected with the segment warping harnesses.<sup>14</sup> The aberrations of these last two cases are based on an analysis of higher-order aberration terms and are discussed more fully in the reference.<sup>11</sup>

Table 2 shows that the analysis performed predicts contrast to within a factor of two for these previously analyzed cases. For all three cases, lower contrasts are predicted than were actually measured. We expect this underestimation because our parametric fit method does not take into account the various cross terms that arise from the combination of multiple aberrations. Given that there remains much uncertainty as to the effectiveness of speckle suppression techniques, this level of prediction still allows the estimation to be a useful tool in the modeling and design of the TMT.

## 5. CONCLUSIONS

We have shown that nulled pupil intensity and image contrast in a segmented nulling interferometer are directly related to the uncorrected wavefront variance. Further-

more, given a set of wavefront correction factors for a set of orthogonal segment aberrations, the nulled pupil intensity after wavefront correction can be accurately predicted. Finally, the results of simulating individual segment aberrations can be combined to easily and accurately predict the total contribution of primary mirror errors. Further improvement in prediction accuracy may be obtained with a more realistic model of the PFI's wavefront control system.

### **Appendix A: Wavefront Correction Disparity**

As shown in Figure 3, the wavefront correction factors achieved with our wave optics adaptive optics simulations are not the same for matched aberration modes such as sine and cosine astigmatism (Z5 and Z6, respectively). This disparity is ultimately due to the geometry of the square grid of actuators and the corresponding shape of the “dark hole” the system carves out in the nulled image plane.

To test this hypothesis, we first used an idealized wavefront correction model. In this model we apply a hard-edged highpass spatial filter to the phase aberrations of the telescope pupil. After this filter all aberrations within the controllable bandpass have been corrected and only higher-order aberrations remain. The wavefront correction factors from this “spatial filter AO” and the ARROYO wave optics AO are plotted in Figure 6. While this simplified model results in overall better wavefront correction for all aberrations, note that the disparity between Z5 and Z6 remains. The key distinctions between these two methods are that the wave-optics system is limited

by (1) imperfect knowledge of the wavefront errors and (2) the pyramid influence functions of a “real” DM.

To quantify this effect we rotated the segment-astigmatic telescope pupil through a series of angles before applying the idealized AO system, computing a correction factor at each orientation. As shown in Figure 7, the correction factors vary regularly every 90 degrees of rotation. As the pupil rotates the power spectral density (PSD) of the wavefront phase also rotates, changing the controllable spatial frequency components. Figure 8 shows the correctable region of the phase PSDs for the two most disparate orientations – clearly at each angle there are different amounts of energy which can be removed from the aberrated PSDs.

Although the wavefront correction factors for the two astigmatism vary a great deal, the correction factor for total segment astigmatism is much more stable. The correction factor for the combination of Z5 and Z6 varies by only about one percent, as shown in Figure 7. The small residual modulation visible results from the hexagonal component of the phase PSD “beating” against the square geometry of the controllable region. Because the aberrations’ total correction factor is constant, the figures in Section 3 plot results as the combination of complementary aberrations.

### **Acknowledgments**

The authors wish to thank Gary Chanan for his valuable comments and assistance, Jerry Nelson for his suggestions on resolving the wavefront correction disparity, and

Stuart Shaklan and Joseph Green for their advice and guidance.

This research was carried out at the Jet Propulsion Laboratory, California Institute of Technology, and was sponsored by the California Institute of Technology and the National Aeronautics and Space Administration. The authors also gratefully acknowledge the support of the TMT partner institutions. They are the Association of Canadian Universities for Research in Astronomy (ACURA), the Association of Universities for Research in Astronomy (AURA), the California Institute of Technology and the University of California. This work was further supported by the Canada Foundation for Innovation, the Gordon and Betty Moore Foundation, the National Optical Astronomy Observatory, which is operated by AURA under cooperative agreement with the National Science Foundation, the Ontario Ministry of Research and Innovation, and the National Research Council of Canada.

## References

1. M. Mayor and D. Queloz, “A Jupiter-Mass Companion to a Solar-Type Star,” *Nature (London)* **378**, pp. 355–359 (1995).
2. R. Neuhauser, M. Mugrauer, and A. Seifahrt, “GQ Lup, 2M1207, and AB Pic: Planet companion candidates imaged directly and their relevance in orbital dynamics and mass estimation via theoretical models,” presented at the International Astronomical Union Symposium on Binary Stars as Critical Tools and Tests in Contemporary Astrophysics, Prague, Czech Republic, 22-25 August.

3. B. Macintosh, J. Graham, D. Palmer, R. Doyon, D. Gavel, J. Larkin, B. Oppenheimer, L. Saddlemyer, J. K. Wallace, B. Bauman, J. Evans, D. Erikson, K. Morzinski, D. Phillion, L. Poyneer, A. Sivaramakrishnan, R. Soummer, S. Thibault, and J.-P. Veran, “The Gemini Planet Imager,” in *Advances in Adaptive Optics II*, B.L. Ellerbroek and D. Bonaccini Calia, eds., Proc. SPIE **6272**, 62720L (2006).
4. B. Macintosh, M. Troy, R. Doyon, J. Graham, K. Baker, B. Bauman, C. Marois, D. Palmer, D. Phillion, L. Poyneer, I. Crossfield, P. Dumont, B. M. Levine, M. Shao, G. Serabyn, C. Shelton, G. Vasisht, J. K. Wallace, J.-F. Lavigne, P. Valee, N. Rowlands, K. Tam, and D. Hackett, “Extreme adaptive optics for the Thirty Meter Telescope,” in *Advances in Adaptive Optics II*, B.L. Ellerbroek and D. Bonaccini Calia, eds., Proc. SPIE **6272**, 62720N (2006).
5. C.A. Beichman, N.J. Woolf, and C.A. Lindensmith, “The terrestrial planet finder (TPF): a NASA origins program to search for habitable planets,” JPL Pub. 99-3 (Jet Propulsion Laboratory, Pasadena, Calif., 1999).
6. B. Mennesson, M. Shao, B. Levine, J. Wallace, D. Liu, E. Serabyn, S. Unwin, and C. Beichman, “Optical Planet Discoverer: How to turn a 1.5m telescope into a powerful exo-planetary systems imager,” in *High-Contrast Imaging for Exo-Planet Detection*, A. Shultz and R. Lyon, eds., Proc. SPIE **4860**, pp. 32–44, (2003).
7. N. Yaitskova and C. Verinaud, “Adaptive optics correction of the wavefront

- distortions induced by segments misalignment in Extremely Large Telescope,” in *Ground-based and Airborne Telescopes*, L.M. Stepp, ed., Proc. SPIE **6267**, 62672N (2006).
8. M. Troy and G. Chanan, “Diffraction effects from giant segmented-mirror telescopes,” *Appl. Opt.* **42**, pp. 3745–3753, (2003).
  9. R. J. Noll, “Zernike polynomials and atmospheric turbulence,” *J. Opt. Soc. Am.* **66**, pp. 207–211 (1976).
  10. M. Britton, “Arroyo,” in *Modeling and Systems Engineering for Astronomy*, S. C. Craig and M. J. Cullum, eds., Proc. SPIE **5497**, pp. 290–300 (2004).
  11. M. Troy, I. Crossfield, G. Chanan, P. Dumont, J. J. Green, and B. Macintosh, “Effects of diffraction and static wavefront errors on high-contrast imaging from the thirty meter telescope,” in *Advances in Adaptive Optics II*, B.L. Ellerbroek and D. Bonaccini Calia, eds., Proc. SPIE **6272**, 62722C (2006).
  12. G. A. Chanan, C. Ohara, and M. Troy, “Phasing the mirror segments of the Keck telescopes II: The narrow-band phasing algorithm,” *Appl. Opt.* **39**, pp. 4706–4714 (2000).
  13. A. Give’on, N. Kasdin, R. Vanderbei, and Y. Avitzour, “On representing and correcting wavefront errors in high-contrast imaging systems,” *J. Opt. Soc. Am. A* **23**, pp. 1063–1073 (2006).
  14. E. Ponslet, D. Blanco, M. Cho, T. Mast, J. Nelson, R. J. Ponchione, M. Sirota,

V. Stephens, L. Stepp, A. Tubb, and E. C. Williams, “Development of the primary mirror segment support assemblies for the Thirty Meter Telescope,” in *Optomechanical Technologies for Astronomy*, E. Atad-Ettinger, J. Antebi, and D. Lemke, eds., Proc. SPIE **6273**, 627319 (2006).

Table 1. Contrast curve coefficients per Eq. (13).

Mode	$\alpha [10^{-4}\text{waves}^2]$
Piston	1.26
Tilt	1.25
Focus	0.83
Astigmatism	2.26
Coma	.67
Trefoil	2.45
Spherical	2.17
Secondary Astigmatism	1.57
Tetrafoil	4.16

Table 2. Predicted TMT PFI contrast for two cases of segment aberrations.

Aberration Case	Predicted Contrast	Measured Contrast
Misalignment Errors	$1.0 \times 10^{-8}$	$1.3 \times 10^{-8}$
Unwarped Surface Errors	$1.2 \times 10^{-7}$	$2.5 \times 10^{-7}$
Warped Surface Errors	$3.0 \times 10^{-8}$	$4.5 \times 10^{-8}$

Fig. 1. Recombined pupils for various visible nuller designs with relative phase shifts labeled. The three types shown are (a) single-shear nuller, (b) perpendicular dual-shear nuller, and (c) parallel dual-shear nuller. The shear distance has been exaggerated for clarity. crossfieldF1.eps

Fig. 2. Obscured TMT primary mirror. crossfieldF2.eps

Fig. 3. Wavefront correction factors for the first fifteen Noll-ordered Zernike modes. crossfieldF3.eps

Fig. 4. Dependence on uncorrected segment aberration level of the (left) mean intensity in the nulled plane and (right) achieved contrast. Both plots exhibit the expected  $\sigma^2$  dependence. Only piston mode is plotted on the left because the different aberrations' curves are indistinguishable. crossfieldF4a crossfieldF4b

Fig. 5. Dependence on segment aberration level after AO correction of the (left) mean intensity in the nulled plane and (right) achieved contrast. Both plots roughly exhibit the expected  $\sigma^2$  dependence. crossfieldF5a.eps crossfieldF5b.eps

Fig. 6. AO correction factors,  $\gamma_k$  using both the full wave-optics simulation described in Section 3.A and the simplified highpass filter correction described in the Appendix. crossfieldF6.eps

Fig. 7. Segment astigmatism correction factors plotted versus initial pupil orientation. Although the Z5 and Z6 correction factors change significantly with rotation, the correction factor for the combined astigmatism is nearly constant. crossfieldF7.eps

Fig. 8. Controllable region of the phase power spectral densities of the Z5 and Z6

segment astigmatism cases, at two different pupil orientations. The total amount of controllable energy in the PSD changes as the pupil rotates, which affects the achieved wavefront correction. crossfieldF8.eps

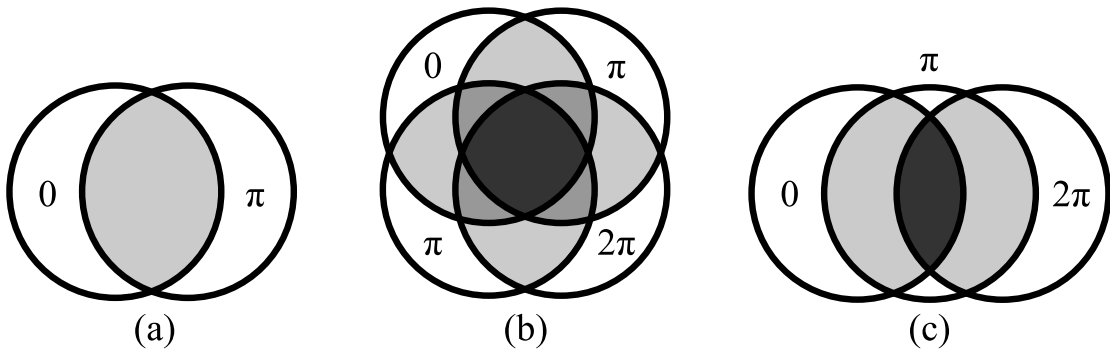


Fig. 1. Recombined pupils for various visible nuller designs with relative phase shifts labeled. The three types shown are (a) single-shear nuller, (b) perpendicular dual-shear nuller, and (c) parallel dual-shear nuller. The shear distance has been exaggerated for clarity. crossfieldF1.eps

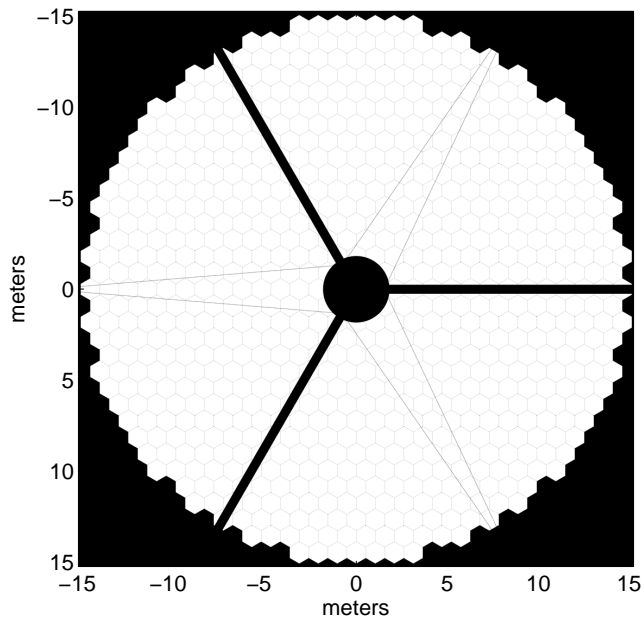


Fig. 2. Obscured TMT primary mirror. crossfieldF2.eps

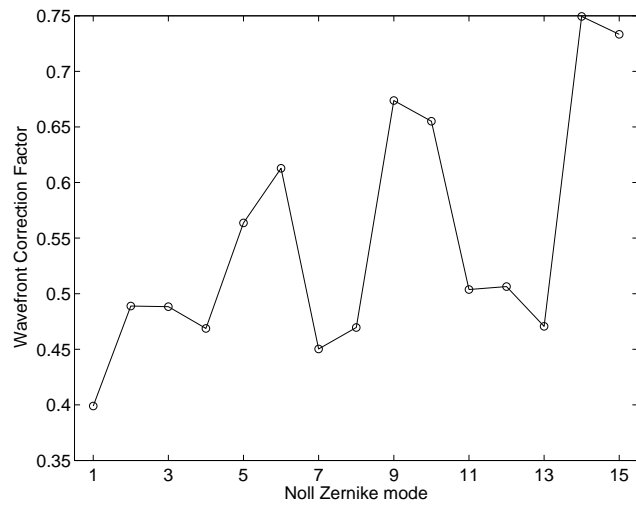


Fig. 3. Wavefront correction factors for the first fifteen Noll-ordered Zernike modes. crossfieldF3.eps

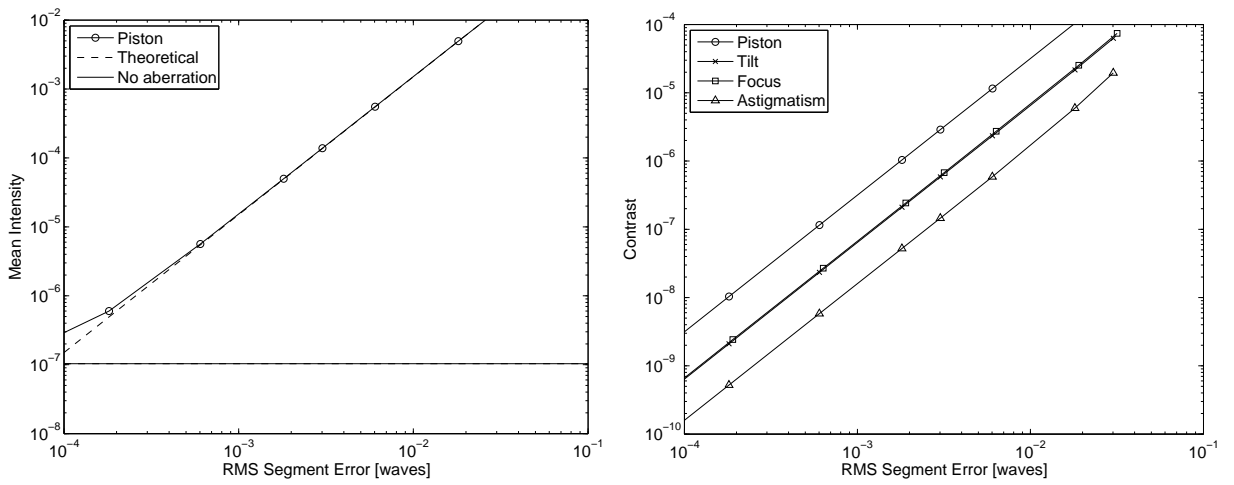


Fig. 4. Dependence on uncorrected segment aberration level of the (left) mean intensity in the nulled plane and (right) achieved contrast. Both plots exhibit the expected  $\sigma^2$  dependence. Only piston mode is plotted on the left because the different aberrations' curves are indistinguishable. crossfieldF4a  
crossfieldF4b

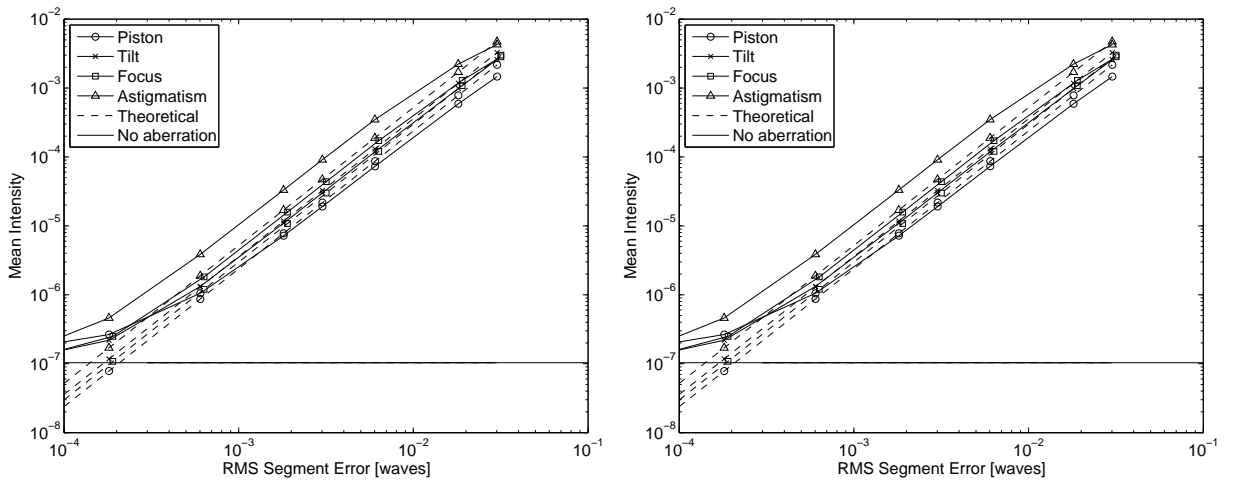


Fig. 5. Dependence on segment aberration level after AO correction of the (left) mean intensity in the nulled plane and (right) achieved contrast. Both plots roughly exhibit the expected  $\sigma^2$  dependence. crossfieldF5a.eps crossfieldF5b.eps

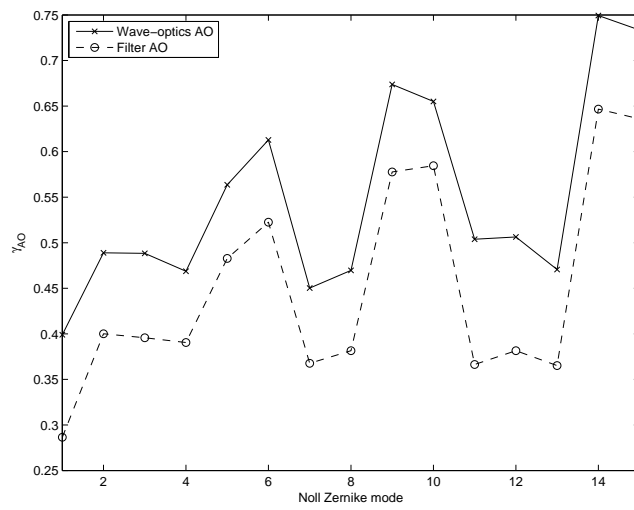


Fig. 6. AO correction factors,  $\gamma_k$  using both the full wave-optics simulation described in Section 3.A and the simplified highpass filter correction described in the Appendix. crossfieldF6.eps

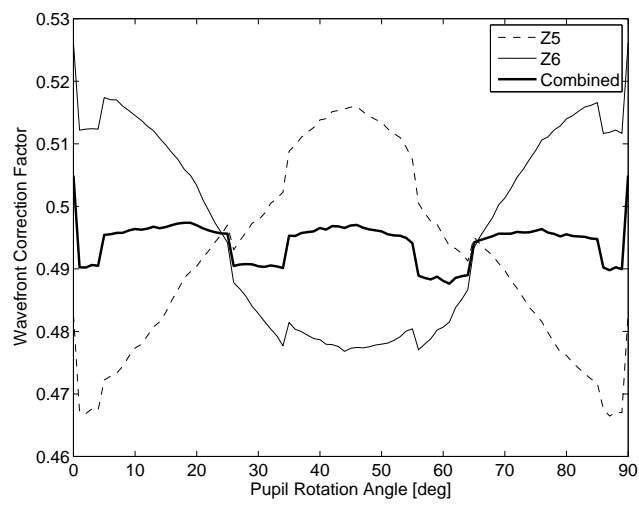


Fig. 7. Segment astigmatism correction factors plotted versus initial pupil orientation. Although the Z5 and Z6 correction factors change significantly with rotation, the correction factor for the combined astigmatism is nearly constant. crossfieldF7.eps

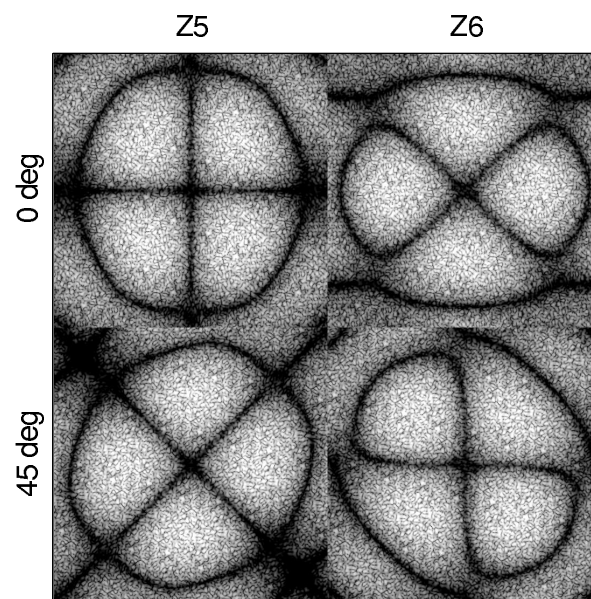


Fig. 8. Controllable region of the phase power spectral densities of the Z5 and Z6 segment astigmatism cases, at two different pupil orientations. The total amount of controllable energy in the PSD changes as the pupil rotates, which affects the achieved wavefront correction. crossfieldF8.eps